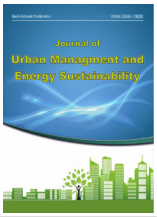
Int. J. Urban Manage. Energy Sustainability, 7(3):244-266, 2026

International Journal of Urban Management and Energy Sustainability (IJUMES)

Homepage: http://www.ijumes.com



ORIGINAL RESEARCH PAPER

A Microdilatational Mixture Theory for Saturated Porous Media: From Virtual Power to Aquitard Compaction and Land Subsidence

Amir Ghiasi Tarzi, Amir Robati*, Mohammad Ali Kazerooni Sadi

Department of Civil Engineering, Ke.C., Islamic Azad university, Kerman, Iran

ARTICLE INFO

Article History:
Received 2026-07-11
Revised 2026-09-10
Accepted 2026-10-18

Keywords:
Aquitard compaction; Land subsidence; Microdilatation continuum; Secondary compression; Theory of Porous Media

ABSTRACT

Groundwater withdrawal drives the compaction of fine-grained aquitards and the resulting land subsidence; however, heavily pumped aquifer systems continue to compact after the excess pore pressure has dissipated, a residual, creep-like settlement that classical Terzaghi–Biot consolidation cannot reproduce and that is usually described by empirical rheological laws. This study aims to provide a thermodynamically consistent, grain-scale origin for this behavior. A microdilatational mixture theory is developed for a saturated medium composed of a solid skeleton, whose grains carry a dissipative dilatational degree of freedom, and a non-polar pore fluid. The balance laws and boundary conditions are derived from the principle of virtual power, the constitutive equations are closed by the Coleman–Noll procedure within the Theory of Porous Media, and the linearized one-dimensional problem is solved with an implicit finite-difference scheme verified against Terzaghi's analytical solution. The grain-scale dilatation relaxes on its own time scale τ_φ, distinct from the drainage time t_c, so that consolidation proceeds in two stages: primary consolidation at the unrelaxed modulus, followed by secondary compression toward the relaxed modulus. For a San Joaquin Valley-type aquitard (h = 20 m, Δh = 30 m), the primary and ultimate settlements are approximately 28 and 72 cm, and under seasonal pumping the internal length scale and relaxation raise the peak phase lag from the classical finite-layer value of 46.6° to approximately 57°. The theory reduces exactly to Biot–Terzaghi poroelasticity and recovers the Taylor–Merchant/Gibson–Lo rheological model in its local limit; its distinctive, testable signatures are the length-scale effects on pore-pressure profiles and on the seasonal phase lag.

DOI: 10.22034/ijumes.2026.2109321.1427

Running Title: A Microdilatational Mixture Theory for Saturated Porous Media

NUMBER OF REFERENCES 40

NUMBER OF FIGURES 05

NUMBER OF TABLES 07

*Corresponding Author:
Email: *Ammirrr@yahoo.com*
Phone: 00983433210043
ORCID: https://orcid.org/0000-0001-5086-5932

INTRODUCTION

Groundwater withdrawal is among the most widespread causes of land subsidence and is, mechanically, a problem of one-dimensional consolidation: as pumping lowers the pore pressure in an aquifer, the bounding fine-grained aquitards slowly drain and compact, and the land surface sinks (Galloway & Burbey, 2011; Herrera-García et al., 2021; Poland, 1984). It is now a recognized global hazard and affects extensive areas of Iran's depleted aquifer systems (Haghshenas Haghighi & Motagh, 2024). Classical Terzaghi–Biot theory ties all compaction to the dissipation of excess pore pressure; for a thick, low-permeability aquitard the drainage time is itself of order years to decades, so the theory does reproduce compaction long after the head stabilizes. What it cannot reproduce is compaction that continues after the excess pore pressure has drained away the residual, creep-like settlement documented in heavily pumped systems (Ojha et al., 2019). The usual remedies are phenomenological: rheological secondary-compression (creep) laws posit a viscoelastic skeleton (Gibson & Lo, 1961; Qi et al., 2025; Taylor & Merchant, 1940), and multi-layer models place the delay in the interbed geometry. Neither derives the skeleton's relaxation from an intrinsic, grain-scale mechanism. This paper supplies such a mechanism through a microdilatational mixture theory: a saturated binary mixture of a solid skeleton whose grains carry a grain-scale dilatational degree of freedom a dissipative internal variable with its own thermodynamically consistent relaxation time and a non-polar elastic pore fluid. That relaxation drives a genuine second stage of consolidation, secondary compression, which continues after primary drainage is complete and which elastic poroelasticity cannot reproduce. The theory combines two classical generalizations of continuum mechanics (Bedford & Drumheller, 1983; Maugin, 2017). Mixture theory (Atkin & Craine, 1976; Truesdell, 1984) represents interpenetrating constituents here a skeleton and a fluid each with its own motion and balance laws, coupled through interaction terms. Micromorphic theory (Eringen, 1999) endows each material point with microstructural degrees of freedom; its microdilatation restriction, limiting the micro-deformation to an isotropic dilatation, is the minimal kinematics that carries a grain-scale volume change while remaining far simpler than the full micromorphic continuum, and it is the natural model of an elastic material with voids (Cowin & Nunziato, 1983; Nunziato & Cowin, 1979). The saturating fluid has no continuum-scale microstructure and is treated as a simple non-polar fluid; endowing it with microstructure would introduce material constants with no physical referent. Among the systematic routes for constructing the balance laws of a generalized continuum (dell'Isola & Placidi, 2011; Del Piero, 2009), we adopt the principle of virtual power (Germain, 1973), which delivers the balance laws and their boundary conditions together and extends transparently to the microstructural fields. The constitutive equations are closed by the Coleman–Noll procedure (Coleman & Noll, 1963; Hütter, 2020) within the Theory of Porous Media (Bowen, 1980; Ehlers, 2002), treating the volume fraction as an internal variable of state. Because the mineral grains are effectively incompressible, the porosity is slaved to the skeleton dilatation and enters as a purely kinematic variable, with the grain-scale response carried instead by the microdilatation.

The two ingredients have so far been developed separately micropolar mixtures within the Theory of Porous Media (Diebels, 2002; Diebels & Ehlers, 1996), micromorphic mixtures (Twiss & Eringen, 1971), and the single-constituent microdilatation continuum (Eringen, 1999) but not combined for a saturated solid–fluid medium. The closest antecedent, Chiriță and Galeș (2008), treated a mixture of two microstretch solids; the present theory differs in that the second constituent is a non-polar fluid (removing microstructural interaction supplies), the volume fraction obeys the TPM saturation constraint, and the balance laws follow from virtual power, which yields their boundary conditions and admissible interactions

simultaneously. The delayed, residual compaction that motivates the application has previously been captured by double-porosity consolidation (Wilson & Aifantis, 1982), dual-porosity creep (Murad et al., 2001), and micro-structured continua with a pore-size length scale (dell'Isola et al., 1998), but through a second diffusing pore pressure rather than the single grain-scale structural field used here; the distinction is drawn in Section 5.4. The contribution is a thermodynamically consistent generalized-continuum theory of saturated porous media, derived from virtual power, that adds one physical ingredient to classical poroelasticity: a dissipative grain-scale degree of freedom with an intrinsic relaxation time. In one-dimensional consolidation this produces a two-stage settlement primary consolidation controlled by drainage, followed by secondary compression that continues after the pore pressure has dissipated. In its spatially local limit this coincides with the classical rheological secondary-consolidation theory of Taylor and Merchant (1940) and Gibson and Lo (1961); the aim here is not to improve that settlement prediction but to supply its missing grain-scale origin and to add what a local rheology cannot: an internal length scale that reshapes the pore-pressure profile near a drainage boundary and produces a seasonal phase lag exceeding the classical finite-layer bound. These length-scale effects are the theory's distinguishing testable content. The specific objectives are threefold: (i) to formulate, from a single variational statement, a thermodynamically admissible mixture theory in which the solid grains carry a dissipative microdilatational degree of freedom; (ii) to verify that it contains Biot–Terzaghi poroelasticity, the theory of elastic materials with voids, and the classical rheological secondary-consolidation model as exact limits; and (iii) to quantify, for a field-representative aquitard, the observable consequences of the new internal time and length scales under monotonic and seasonal withdrawal. The paper is organized as follows. Section 2 describes the methodology and assumptions; Section 3 sets out the non-polar binary mixture (linearization in Appendix A); Section 4 develops the microdilatation continuum (Appendix B); Section 5 combines them into the microdilatational mixture theory, verifying the poroelastic and voids limits (Appendix C); Section 6 applies the linearized theory to one-dimensional consolidation and land subsidence, including verification, sensitivity and limitations; and Section 7 concludes.

Methodology

This study follows a theoretical–computational design that proceeds from first principles to a verified, field-scale application (Fig. 1), in two parts. Part A (Stages 1–4) constructs the continuum theory deductively, so that every field equation, boundary condition and constitutive relation follows from stated kinematic and thermodynamic postulates. The porous medium is idealized as a saturated binary mixture of a solid skeleton and a pore fluid within the Theory of Porous Media (Bowen, 1980; Ehlers, 2002), with only the solid carrying microstructure, restricted to an isotropic grain-scale dilatation $\chi(s) = \beta(s)1$ (Eringen, 1999; Nunziato & Cowin, 1979). The balance laws and natural boundary conditions are obtained simultaneously from the principle of virtual power (Germain, 1973) first for the non-polar mixture (Section 3), then for the microdilatation continuum (Section 4), then for their combination (Section 5) with objectivity identifying the admissible interaction terms. Constitutive closure follows from the Coleman–Noll exploitation of the free-energy imbalance (Coleman & Noll, 1963; Hütter, 2020); splitting the residual dissipation into equilibrium and non-equilibrium parts produces the Darcy drag and a dissipative equilibrated body force that endows the microdilatation with an intrinsic relaxation time. The equations are then linearized about a stress-free reference state (Appendices A–C) and checked against three exact limits: Biot–Terzaghi poroelasticity, elastic materials with voids, and the elliptic microdilatation theory. Part B (Stages 5–8) specializes the linear theory to the one-dimensional

compaction of a singly drained aquitard under a step decline, or harmonic oscillation, of the adjacent aquifer head (Section 6.1). Scaling identifies three dimensionless groups the coupling ratio βB, the length ratio $\Lambda = l/h$ and the time ratio $R = \tau\varphi/tc$. The coupled parabolic system for the pore pressure and the microdilatation is discretized by central finite differences and integrated with the unconditionally stable Backward-Euler scheme, with the seasonal periodic response computed in the frequency domain; the solver is verified against the closed-form Terzaghi series solution in the appropriate limits and by mesh and time-step refinement. The results are then interpreted in terms of the two-stage settlement, the pore-pressure boundary layer and the seasonal phase lag, and their sensitivity to βB and R, using field-representative parameters from the San Joaquin Valley, California, the best-documented aquifer system for pumping-induced subsidence (Galloway & Burbey, 2011; Lees et al., 2022; Ojha et al., 2019).

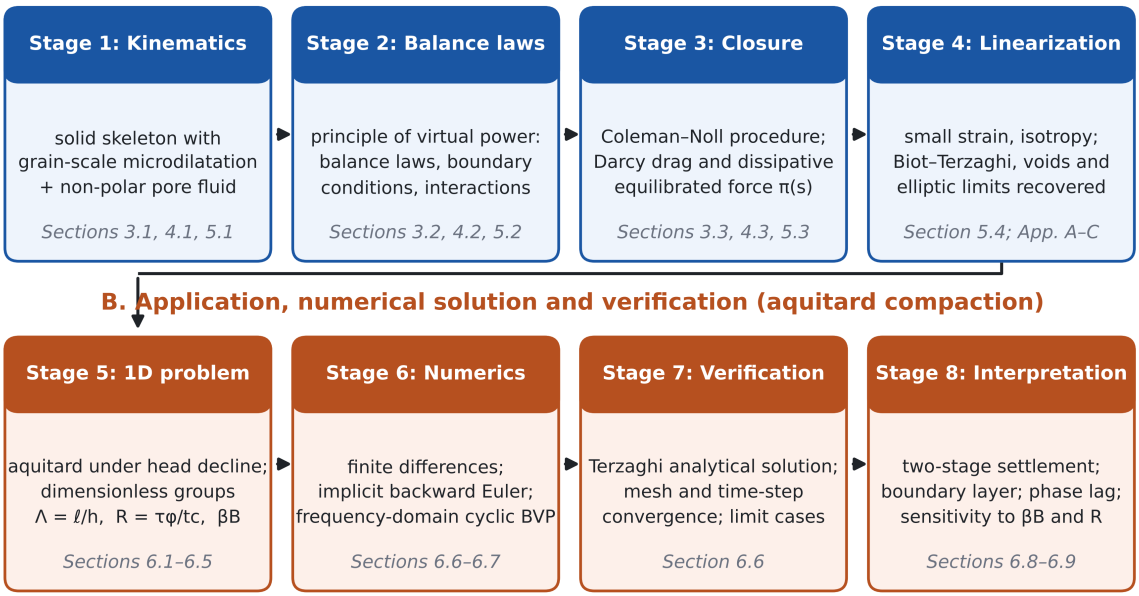


Figure 1: Research methodology. Part A (Stages 1–4) derives the microdilatational mixture theory from kinematic and thermodynamic postulates; Part B (Stages 5–8) applies it to pumping-induced aquitard compaction, solves and verifies the resulting boundary-value problem, and interprets the results. The sections in which each stage is carried out are indicated in each box.

The modelling assumptions adopted at each stage, their justification and the way in which they could be relaxed are summarized in (Tab. 1). They define the domain of validity of the results reported in Section 6.

Table 1: Principal modelling assumptions, their justification and their status in the present study.

Assumption	Justification	Consequence / possible relaxation
Saturated binary mixture; no mass exchange	Aquitards below the water table are fully saturated	Mass supply in (5) would admit reactive or phase-changing media
Materially incompressible grains	Standard for water-saturated clays and silts (Ehlers, 2002)	Porosity is slaved to skeleton dilatation; no double counting
Microstructure restricted to isotropic dilatation, $\chi(s) = \beta(s)1$	Minimal kinematics carrying grain-scale volume change	Full micromorphic or micropolar kinematics possible

Non-polar, inviscid pore fluid	No pore-fluid microstructure at the continuum scale	Viscosity enters only through the Darcy drag
Quasi-static loading	Pumping time scales ≫ wave transit times	Dynamic analysis would yield dispersive waves
Small strains, isotropic linear response	Aquitard strains of order 10−2	Large-strain and anisotropic extensions
One-dimensional, singly drained layer	Classical interbed idealization	Multi-layer, doubly drained systems
Incompressible-constituent limit $\kappa f \to \infty$ in Section 6	Fluid compressibility ≪ skeleton compressibility	Retaining κf adds a storage term

Continuum mixture theory

This section establishes the two-constituent poroelastic baseline of the theory. It is deliberately standard, a non-polar solid skeleton saturated by a pore fluid, so that the microstructural effects introduced from Section 4 onward are cleanly attributable to the microdilatation kinematics rather than to the mixture description itself. The balance laws and effective-stress structure recovered here are those of the classical Theory of Porous Media (Atkin & Craine, 1976; Bowen, 1976; Ehlers, 2002; Truesdell, 1984); we recapitulate them compactly via the principle of virtual power, both to fix notation and because the same variational argument carries unchanged into the microdilatation mixture of Section 5. Throughout, superscripts (s) and (f) label the solid and fluid constituents; the principal symbols are collected in (Tab. 2).

Table 2: Principal notation.

Symbol	Meaning
$\phi^{(\alpha)}$, $X^{(\alpha)}$	motion of constituent α; reference (material) position
$n^{(\alpha)}$	volume fraction of constituent α ($n^{(s)}+n^{(f)}=1$)
$\rho^{(\alpha)}$, $\rho^{R(\alpha)}$	partial and real (intrinsic) mass density
$v^{(\alpha)}$, $v^{(fs)}$	constituent velocity; seepage velocity $v^{(f)}-v^{(s)}$
$u^{(\alpha)}$	displacement of constituent α
grad, div	spatial gradient and divergence (w.r.t. x)
Grad, Div	referential gradient and divergence (w.r.t. X)
$F^{(s)}$, $C^{(s)}$	solid deformation gradient; right Cauchy–Green tensor
$\chi^{(s)}$	solid micro-deformation tensor
$\beta^{(s)}$, $\varphi^{(s)}$	scalar microdilatation ratio; perturbation $\beta^{(s)}-1$
$\varepsilon^{(s)}$, $e_l^{(s)}$	linear solid strain; microdilatation strain
$K^{(s)}$	microdilatation gradient
$T^{(\alpha)}$	partial (force) stress
$s^{(s)}$, $m^{(s)}$	scalar microdilatation stress; microdilatation double-stress
$t^{(\alpha)}$, n	partial traction vector; outward unit normal
$pl^{(\alpha)}$	momentum supply (interaction force)
$b_0^{(\alpha)}$, l_d	body force; microdilatation body action
$\psi^{(\alpha)}$, $D^{(\alpha)}$	Helmholtz free energy; rate of deformation
p_{th}, B	thermodynamic pore pressure; drag tensor
$\lambda^{(s)}$,$\mu^{(s)}$	drained Lamé moduli

$a^{(s)}, b^{(s)}, c_1^{(s)}$	microdilatation moduli and length-scale modulus
κ_f, k	fluid bulk modulus; hydraulic mobility ($k=K_v/\gamma_w$)
K_v, γ_w	vertical hydraulic conductivity; unit weight of water
$\bar{M}$, B^-, A^-	effective oedometric, coupling, and microdilatation moduli
$\bar{M}$, $\bar{M}_{eff}$, β_B	unrelaxed and relaxed oedometric moduli; coupling ratio
$\omega^{(s)}$, τ_φ, R	equilibrated-force dissipation; relaxation time $\omega^{(s)}/(3A^-)$; ratio τ_φ/t_c
c_v, t_c, l, Λ	consolidation coefficient $k\bar{M}$; drainage time h^2/c_v; length scale; ratio l/h
h, Δp_0, S	aquitard thickness; head-decline pressure; subsidence

FINDINGS AND DISCUSSION

The two-constituent poroelastic baseline and the single-constituent microdilatation continuum are standard building blocks; their full derivations are provided in Appendix A and Appendix B, respectively. The main text proceeds directly to the microdilatational mixture theory that combines them.

Microdilatational mixture theory

Combining the mixture framework of Section 3 with the microdilatation continuum of Section 4 yields the central object of the paper: a saturated mixture of a solid skeleton whose grains carry a microstructural dilatation, an elastic material with voids (Cowin & Nunziato, 1983; Nunziato & Cowin, 1979), and a non-polar pore fluid. Generalized-continuum solid–fluid mixtures have been formulated before, notably the micropolar mixture of Diebels (2002); the contribution here is a mixture that couples the grain-scale dilatational degree of freedom to a non-polar pore fluid within the Theory of Porous Media, derived throughout by the principle of virtual power. It is the poroelastic (fluid-saturated) extension of the theory of elastic materials with voids.

Kinematics of the microdilatational mixture

We consider a binary mixture in which only the solid constituent $\alpha=s$ carries microdilatation kinematics. The solid micro-deformation tensor is restricted to the pure-dilatation form

$$\chi^{(s)}=\beta^{(s)}1, \tag{36}$$

with purely spherical micro-gyration, as in (23),

$$\upsilon^{(s)}=1/\beta^{(s)}\left(d^{(s)}\beta^{(s)}\right)/dt\,1. \tag{37}$$

The fluid constituent $\alpha=f$ is a standard non-polar fluid: it carries only translational kinematics (velocity field $v^{(f)}$) with no grain-level microstructure, the physically appropriate model for a pore fluid.

The scalar microdilatation ratio $\beta^{(s)}$ of the solid carries a concrete physical meaning. As the saturating fluid moves into or out of the pore space, or is absorbed into and expelled from the microporous solid itself, the change in local fluid content induces an isotropic volumetric change of the solid skeleton at the grain level: the microstructural elements swell as fluid is taken up and contract as it is released. This grain-level isotropic dilatation is precisely what $\beta^{(s)}$ tracks: it is the microstructural degree of freedom that distinguishes the theory from classical poroelasticity, providing a kinematic description of the coupling between pore-fluid content and solid microstructure that the macroscopic deformation gradient $F^{(s)}$ cannot capture alone.

Mechanical fields and balance laws

Since only the solid carries microdilatation kinematics, the virtual power structure of Section 4.2 applies to the solid constituent with label (s) appended, while the fluid contributes only a translational virtual power. The sole interaction between the two constituents is the linear momentum supply $pl^{(\alpha)}$: since the fluid is non-polar, no microdilatation-momentum production acts on the solid from the fluid (Diebels, 2002).

The virtual power of internal forces for the solid generalizes (24) as

$$P_i^{(s)} = \int_{\mathcal{P}(s)} [\ \mathbf{T}^{(s)}:\mathbf{D}^{*(s)} + s^{(s)}(\mathrm{tr}\mathbf{L}^{*(s)} - 3\,(1/\beta^{(s)}\,d^{(s)}\beta^{(s)}/dt)^{*}) + \mathbf{m}^{(s)}\cdot \mathrm{grad}(1/\beta^{(s)}\,d^{(s)}\beta^{(s)}/dt)^{*}]\,dv \quad (38)$$

and the virtual power of internal forces for the non-polar fluid is simply

$$P_i^{(f)} = \int_{\mathcal{P}(f)} \mathbf{T}^{(f)} : \mathbf{D}^{*(f)}\ dv, \quad (39)$$

Applying the divergence theorem and equating with the external virtual power, which includes the linear momentum supply pl^{α} for both constituents, gives the local balance laws:

$$\mathrm{div}\left(\mathbf{T}^{(s)} + s^{(s)}\mathbf{1}\right) + \mathbf{b}_0^{(s)} + \mathbf{pl}^{(s)} = \mathbf{0} \quad (40)$$

$$\mathrm{div}\mathbf{m}^{(s)} + 3s^{(s)} + l_d^{(s)} = 0 \quad (41)$$

$$\mathrm{div}\mathbf{T}^{(f)} + \mathbf{b}_0^{(f)} + \mathbf{pl}^{(f)} = \mathbf{0} \quad (42)$$

with boundary conditions $\mathrm{t}^{s}=(\mathrm{T}^{s}+s^{s}1)\cdot n$, $\mathrm{m}^{s}_{d})=\mathrm{m}^{s}n$, $\mathrm{t}^{f}=\mathrm{T}^{f}\cdot n$. The solid force stress $\mathrm{T}^{(s)}$ is symmetric, so angular momentum is satisfied identically and no couple stress arises; the microdilatation-momentum balance (41) takes the same form as the single-constituent balance of Section 4.2 with label (s), carrying no interaction supply from the fluid.

Objectivity of the total mixture virtual power under a superposed rigid-body motion requires only the linear momentum constraint

$$\mathrm{pl}^{s}+\mathrm{pl}^{f}=0. \quad (43)$$

Equation (43) is the mixture-level linear-momentum balance; no microdilatation-momentum mixture constraint arises because the fluid carries no corresponding degree of freedom.

Free-energy inequality and constitutive equations

The mixture free-energy inequality for the microdilatation solid saturated by the non-polar fluid reduces to

$$\rho^{(s)}\frac{d^{(s)}\psi^{(s)}}{dt} + \rho^{(f)}\frac{d^{(f)}\psi^{(f)}}{dt} - \mathbf{T}^{(s)}:\mathbf{D}^{(s)} - \mathbf{T}^{(f)}:\mathbf{D}^{(f)} - s^{(s)}\left(\mathrm{tr}\mathbf{L}^{(s)} - 3\,\frac{1}{\beta^{(s)}}\frac{d^{(s)}\beta^{(s)}}{dt}\right) - \mathbf{m}^{(s)}\cdot\mathrm{grad}\left(\frac{1}{\beta^{(s)}}\frac{d^{(s)}\beta^{(s)}}{dt}\right) + \mathbf{pl}^{(f)}\cdot\mathbf{v}^{(fs)} \le \quad (44)$$

The single seepage dissipation term $\mathrm{pl}^{f}.\mathrm{v}^{fs}$) represents the energy dissipated by relative translational flow between the constituents.

We adopt the solid strain measures (29)– (30) evaluated for the solid phase, with free energies

$$\psi^{(s)}=\psi^{(s)}(C^{(s)},e^{(s)},K^{(s)}),\ \ \psi^{(f)}=\psi^{(f)}(\rho^{R(f)}). \quad (45)$$

The microdilatation β^{s} describes the grain-scale structural dilatation of the skeleton, the local rearrangement and change of micro-void space, at constant grain-material density; it does not represent compression of the incompressible solid material assumed in Section 3.3, and is therefore an independent, energetically active degree of freedom (Cowin & Nunziato, 1983; Nunziato & Cowin, 1979). Consistent with Section 3.3, the solid free energy ψ^{s} does not depend on the volume fraction n^{s}: the grain-scale structural response is carried by the measures (e^{s},K^{s}), while n^{s} remains the kinematic fluid-content variable, so that the porosity energetics is not double-counted. Applying the Coleman–Noll procedure to (44) yields the symmetric solid force stress and microdilatation stresses:

$$\mathbf{T}^{(s)} = 2\rho^{(s)}\,\mathbf{F}^{(s)}\cdot\frac{\partial\psi^{(s)}}{\partial\mathbf{C}^{(s)}}\cdot\left(\mathbf{F}^{(s)}\right)^{T} - p_{th}\,n^{(s)}\,\mathbf{1} \quad (46)$$

$$s^{(s)} = \rho^{(s)}\,e^{(s)}\,\frac{\partial\psi^{(s)}}{\partial e^{(s)}} \quad (47)$$

$$\mathbf{m}^{(s)} = \rho^{(s)}\,\frac{\partial\psi^{(s)}}{\partial\mathbf{K}^{(s)}}\cdot\left(\mathbf{F}^{(s)}\right)^{T} \quad (48)$$

with p_{th} defined as in (14); as in Section 3.3 no configurational pressure appears, since ψ^{s} is independent of n^{s}. The residual dissipation inequality then yields the fluid split

$$T^{f}=-nfp_{th}\,1, \quad (49)$$

$$pl^{(f)Eq}=p_{th}gradn^{(s)} \quad (50)$$

$$pl^{(f)NEq}\&=-B.v^{(fs)}$$

with B positive semi-definite. The residual inequality admits, in addition, a dissipative equilibrated body force π^s conjugate to the microdilatation rate $\beta^{-1}\, d^s\, \beta/dt$, in the manner of Nunziato and Cowin (1979) and Cowin and Nunziato (1983) and exactly parallel to the way the Darcy drag arises from the seepage dissipation. Requiring the associated dissipation to be non-negative in every process yields the linear law

$$\pi^{(s)} = -\omega^{(s)} \frac{1}{\beta^{(s)}} \frac{d^{(s)}\beta^{(s)}}{dt} \qquad \omega^{(s)} \geq 0 \tag{51}$$

with ω^s a single new material constant, so that the dissipation is $-\pi^{(s)}\,(\beta^{-1}\, d^{(s)}\,\beta/dt)=\omega^s\,(\beta^{-1} d^{(s)}\,\beta/dt)^2 \geq 0$. Unlike the Cauchy and microdilatation stresses (46)–(48), which remain rate-independent, π^s is a dissipative body action: it enters the microdilatation balance (41) additively, which with dissipation reads $\mathrm{div}\mathbf{m}^{(s)}+3s^{(s)}+\pi^{(s)})+l_d^{(s)})=0$, and renders it parabolic on linearization (Section 6). As in Section 3.3 the pore fluid is inviscid, so its stress is the pure pore pressure and all seepage dissipation is carried by the Darcy drag. Equations (46)–(50) close the microdilatational mixture theory: given $\psi^{(s)}$, $\psi^{(f)}$, B, the field equations (40)–(42) together with these constitutive relations determine the coupled solid motion, grain-scale dilatation, and fluid seepage.

For small strains and isotropic solid response, these reduce to the linear voids-poroelastic constitutive equations. The solid stresses are

$$\mathbf{T}^{(s)} = \lambda^{(s)}\big(\mathrm{tr}\boldsymbol{\varepsilon}^{(s)}\big)\mathbf{1} + 2\mu^{(s)}\boldsymbol{\varepsilon}^{(s)} + b^{(s)}\, e_1^{(s)}\,\mathbf{1} - n_0^{(s)}\, p_{th}\,\mathbf{1} \tag{52}$$

$$s^{(s)} = a^{(s)}\, e_1^{(s)} + b^{(s)}\,\mathrm{tr}\boldsymbol{\varepsilon}^{(s)} \tag{53}$$

$$\mathbf{m}^{(s)} = c_1^{(s)}\,\mathbf{K}^{(s)} \tag{54}$$

and the fluid relations are

$$p_{th} = -\kappa_f\,\mathrm{Div}\mathbf{u}^{(f)} \tag{55}$$

$$\mathbf{T}^{(f)} = -n_0^{(f)}\, p_{th}\,\mathbf{1} \tag{56}$$

$$\mathbf{pl}^{(f)} = p_{th}\,\mathrm{Grad}\tilde{n}^{(s)} - \frac{1}{k}\,\mathbf{v}^{(fs)} \tag{57}$$

where $\varepsilon^{(s)}=1/2\ (\mathrm{Grad}\mathbf{u}^{(s)} + (\mathrm{Grad}\mathbf{u}^{(s)})^T)$ is the symmetric solid strain, $e_1^{(s)}=\mathrm{Div}\mathbf{u}^{(s)} - 3\varphi^{(s)}$ the microdilatation strain, $\mathbf{K}^{(s)}=\mathrm{Grad}\varphi^{(s)}$ the microdilatation gradient, $\varphi^{(s)}=\beta^{(s)}-1$ the microdilatation perturbation, and $\tilde{n}^{(s)}=n^{(s)} - n_0^{(s)}$. The solid moduli $\lambda^{(s)}$, $\mu^{(s)}$, $a^{(s)}$, $b^{(s)}$, $c_1^{(s)}$ are those of the microdilatation continuum (Appendix B), κ^f is the fluid bulk modulus, $n_{(s)}$ the reference solid volume fraction, and k the hydraulic mobility. The solid stress (52) is the elastic-with-voids stress augmented by the Biot pore-pressure coupling $-n_0^{(s)}\, p_{-th}\,1$; setting the microdilatation moduli to zero recovers the linear Biot–Terzaghi poroelasticity of Section 3.3. The linearization and the Coleman–Noll derivation of (52)–(57) are given in Appendix C. The scalar stress (53) is rate-independent; the dissipative equilibrated body force $\pi^{(s)} = -\omega^{(s)}\,\dot{\varphi}^{(s)}$ of (51) enters the microdilatation balance (41) separately and renders it parabolic, as used in Section 6.

Special cases and relation to poroelasticity with voids

Two reductions locate the theory. First, switching off the microdilatation ($\beta^{(s)}\equiv 1$, equivalently $a^{(s)}=b^{(s)}=c_1^{(s)}=0$ and $\varphi^{(s)}=0$) removes $s^{(s)}$ and $\mathbf{m}^{(s)}$ from (40)–(41), and the theory collapses to the classical non-polar solid–fluid mixture of Section 3, i.e. linear Biot–Terzaghi poroelasticity in the small-strain limit.

Second, retaining the microdilatation but removing the fluid ($p_{th}\to 0$, $\mathbf{pl}^{(s)}\to 0$) recovers the single-constituent microdilatation continuum of Section 4, the theory of elastic materials with voids of Nunziato and Cowin (1979) and Cowin and Nunziato (1983), with $\varphi^{(s)}=\beta^{(s)}-1$ in the role of the void-volume fraction. The present theory is thus the saturated, fluid-coupled (poroelastic) extension of the elastic-materials-with-voids theory, obtained within the Theory of Porous Media from a single variational statement. This places the theory within, but distinct from, the established literature on porous media with a second structural or storage field. The theory of consolidation with double porosity (Wilson & Aifantis, 1982) and its dual-porosity homogenization into secondary compression and hereditary creep (Murad

et al., 2001) likewise predict a delayed, two-time-scale settlement that reduces to classical Terzaghi consolidation in the single-porosity limit, and micro-structured continua with an internal pore-size length scale have been used to model the compaction of fluid-saturated grounds (dell'Isola et al., 1998). The essential difference is mechanistic: in those theories the second field is a second, diffusing pore pressure governed by a storage–transport equation, whereas here it is a grain-scale structural degree of freedom of the solid, governed by the relaxational balance (41) and driven directly by the displacement field. Both yield a two-time-scale settlement with a secondary-compression stage; the present theory locates the second time scale in an intrinsic grain-scale relaxation τ_φ rather than in the drainage of a second pore network. In this respect the theory is closer to the voids-based double-porosity thermoelasticity of Ieşan and Quintanilla (2014), in which, as here, the porosity structure is driven directly by the displacement field rather than by Darcy diffusion. The main similarities and differences between these descriptions and the present theory are summarized in (Tab. 3). The consolidation application of Section 6 uses this theory directly.

Table 3: Comparison of the present theory with alternative continuum descriptions of delayed (secondary) compaction.

Model	Additional field or mechanism	Time scales	Internal length	Basis of derivation
Terzaghi–Biot poroelasticity (Biot, 1941; Terzaghi, 1943)	None	t_c	No	Poroelastic balance laws
Rheological secondary consolidation (Gibson & Lo, 1961; Taylor & Merchant, 1940)	Posited spring–dashpot skeleton	t_c, rheological relaxation time	No	Phenomenological
Double porosity (Wilson & Aifantis, 1982)	Second, diffusing pore pressure	t_c, interporosity exchange time	No	Mixture theory, two pore networks
Dual-porosity homogenization (Murad et al., 2001)	Micro-pore pressure; hereditary creep	t_c, micro-drainage time	Implicit (cell size)	Homogenization
Micro-structured continuum (dell'Isola et al., 1998)	Pore-size scale parameter	t_c	Yes (pore size)	Micro-structured continuum
Present theory	Grain-scale microdilatation $\varphi(s)$	t_c, τ_φ	Yes, l	Virtual power + Coleman–Noll (TPM)

Application: Aquitard Compaction and Land Subsidence from Groundwater Withdrawal

As a physically concrete application we analyze the compaction of a saturated clay/silt aquitard and the land subsidence it produces when the head in an adjacent aquifer is lowered by groundwater withdrawal. Mechanically, this subsidence is the one-dimensional consolidation of the fine-grained interbeds (Galloway & Burbey, 2011; Poland, 1984; Terzaghi, 1943). As pumping lowers the pore pressure at the aquitard boundary, the excess pressure trapped in the low-permeability layer bleeds off slowly. The effective stress then rises, the layer compacts, and the land surface drops. Here the grain-scale dilatation $\varphi^{(s)}$ should matter. Thick aquitards keep compacting long after the driving head has stabilized. Part of this delay reflects the slow drainage of thick interbeds, which classical theory captures (Lees et al., 2022); what it does not reproduce is the residual compaction that continues after the excess pore pressure has dissipated (Ojha et al., 2019).

We consider a compressible aquitard occupying $0 \le z \le h$, drained at the top boundary $z=h$ toward the depressurized aquifer and bound-

ed below at z=0 by an effectively impermeable, rigid base (an aquiclude); see (Fig. 2). At t=0 the aquifer head is lowered by Δh, imposing a pore-pressure decline Δp_0=γ_wΔh at the drained boundary; the total overburden stress is held constant. All fields depend only on z and t. We restrict to purely isotropic compression, and the active fields are the solid displacement $u^{(s)}(z,t)$, the fluid displacement $u^{(f)}(z,t)$, and the scalar microdilatation perturbation $\varphi^{(s)}(z,t)=\beta^{(s)}-1$. The only microstructural field is the scalar dilatation $\varphi^{(s)}$. Because the total stress is constant and the drive enters through the boundary pore pressure, the governing equations coincide with those of classical one-dimensional consolidation under a step load of magnitude q=Δp_0. The land subsidence is the resulting compaction of the layer, $S(t)=-u^{(s)}(h,t)=\int_0^h [-\partial_z u^{(s)}]\, dz$

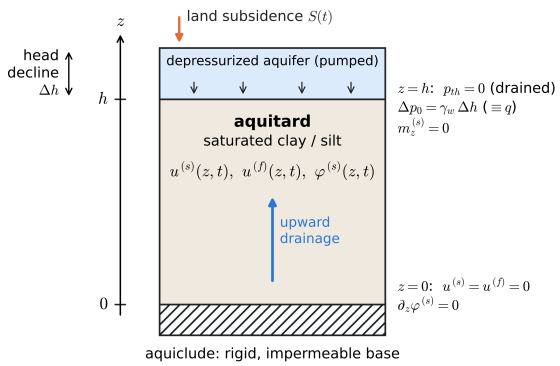


Figure 2: Definition sketch for the one-dimensional consolidation problem. A saturated aquitard of thickness h occupies 0 ≤ z ≤ h, drained at the top (z = h) toward a depressurized aquifer and bounded below (z = 0) by a rigid, impermeable aquiclude. Groundwater withdrawal lowers the aquifer head by Δh, imposing a pore-pressure decline Δp0 = γwΔh at the drained boundary while the total overburden stress is held constant; excess pore pressure drains upward, the layer compacts, and the land surface subsides by S(t). The active fields are the solid and fluid displacements u(s), u(f) and the grain-scale microdilatation φ(s).

We adopt the following standard consolidation simplifications: volume-fraction gradient terms in the momentum supply are neglected. The pore fluid is already inviscid (Section 3.3), so seepage is resisted by interfacial Darcy drag alone. The thermodynamic pressure reduces to

$$p_{th}=-\kappa_f \partial_z u^{(f)} \tag{58}$$

and for notational compactness we define three effective moduli:

$$\bar{M}:=\lambda^{(s)}+2\mu^{(s)}+2b^{(s)}+a^{(s)} \qquad \bar{B}:=3\left(a^{(s)}+b^{(s)}\right) \qquad \bar{A}:=3a^{(s)} \tag{59}$$

where M^- is the effective oedometric modulus, B^- measures the volumetric–microdilatation coupling, and A^- is the microdilatation bulk stiffness (the moduli $a^{(s)}$, $b^{(s)}$ are defined in Appendix C).

Governing equations

In 1D, the linearized strain measures (Appendix C) reduce to

$$\varepsilon^{(s)}=\partial_z u^{(s)} \qquad e_1^{(s)}=\partial_z u^{(s)}-3\varphi^{(s)} \qquad K^{(s)}=\partial_z \varphi^{(s)}, \tag{60}$$

With $n^{(s)}\approx 0$, the zz-component of the linearized solid stress (52) and the microdilatation stress (53) give

$$T_{zz}^{(s)}+s^{(s)} = \bar{M}\,\partial_z u^{(s)}-\bar{B}\,\varphi^{(s)}-n_0^{(s)}\,p_{th} \tag{61}$$

$$m_z^{(s)} = c_1^{(s)}\,\partial_z \varphi^{(s)} \tag{62}$$

and the (inviscid) fluid partial stress is $T_{zz}^{(f)}=n_0^{(f)}\kappa_f \partial_z u^{(f)}$.

Since $T^{(s)}$ is symmetric, the quasi-static balance laws reduce in 1D to three equations:

$$\partial_z\left[\bar{M}\,\partial_z u^{(s)}-\bar{B}\,\varphi^{(s)}\right]-n_0^{(s)}\,\partial_z p_{th}-1/k\left(\partial_t u^{(s)}-\partial_t u^{(f)}\right) = 0 \tag{63}$$

$$-n_0^{(f)}\,\partial_z p_{th}+\frac{1}{k}\left(\partial_t u^{(s)}-\partial_t u^{(f)}\right) = 0 \tag{64}$$

$$\omega^{(s)}\partial_t \varphi^{(s)}=c_1^{(s)}\partial_{zz}\varphi^{(s)} \tag{65}$$

In (63)–(64) the pore-pressure terms $-n_0^{(\alpha)}\partial_z p_{th}$ are the divergences of the Biot partial stresses (61), (20), and the Darcy drag $\pm k^{-1}(\partial_t u^{(s)}-\partial_t u^{(f)})$ satisfies the mixture constraint (43); the geometric factor $n_0^{(f)}$ is tracked explicitly in the derivation of (67) below. Equation (65) is the linearized microdilatation balance (41) for the solid, carrying the dissipative equilibrated

body force $-\omega^{(s)}\,\partial_t\,\varphi^{(s)}$ of (51), the microdilatational counterpart of the Darcy drag. It renders the balance parabolic in $\varphi^{(s)}$: the grain-scale dilatation relaxes over its own characteristic time rather than adjusting instantaneously to $u^{(s)}$. Thermodynamic consistency requires only $\omega^{(s)}\geq 0$, since the residual dissipation is $\omega^{(s)}(\partial_t\,\varphi^{(s)})^2\geq 0$, the one-sided inequality that also governs the Darcy mobility $k>0$. In the limit $\omega^{(s)}\to 0$ the balance degenerates to the elliptic (equilibrated) form and $\varphi^{(s)}$ is slaved to $u^{(s)}$ instantaneously.

Adding (63) and (64) eliminates Darcy drag, and integrating once with the boundary condition at z=h gives the mixture integral

$$\bar{M}\;\partial_z u^{(s)} - \bar{B}\,\varphi^{(s)} - p_{th} = -q,$$

Differentiating (66) in time gives $\partial_t\,p_{th}=M\,\partial_z\,\partial_t\,u^{(s)}-B\partial_t\,\varphi^{(s)}$. We eliminate the seepage velocity using the fluid balance (64) and the pressure–strain relation (58). In the incompressible-constituent limit $\kappa_f\to\infty$ the fluid storage term $-\partial_t\,p_{th}/\kappa_f$ vanishes and the saturation constraint ties the fluid volume flux to the skeleton dilatation rate, leaving $\partial_z\,\partial_t\,u^{(s)}=k(n_0^{(f)})^2\,\partial_{zz}\,p_{th}$. Because the Darcy flux is $n_0^{(f)}v^{(fs)}$, Darcy's law is recovered when the drag coefficient 1/k in (20) equals $(n_0^{(f)})2\gamma_w/K_v$, as is standard in the Theory of Porous Media (Ehlers, 2002); that is, the product $k(n_0^{(f)})^2$ is the hydraulic mobility K_v/γ_w. Writing k for this product hereafter (as in Table 2 and Section 6.6; the dimensionless results are unaffected) then gives the modified consolidation equation:

$$\partial_t\,p_{th}=c_v\,\partial_{zz}\,p_{th}-B^{-}\partial_t\,\varphi^{(s)}),\quad c_v:=k\bar{M}. \tag{67}$$

where $\partial_t\,\varphi^{(s)}$ is now governed by the evolution equation (65). Equations (67) and (65) with the mixture integral (66) form a coupled parabolic–parabolic system for $(p_{th},\varphi^{(s)})$: the pore pressure evolves under drainage on the time scale $t_c=h^2/c_v$, while the microdilatation relaxes on the independent time scale τ_φ of (76) below. The relaxed modulus $\bar{M}_{eff}$ obtained below is the late-time ($t\gg\tau_\varphi$) stiffness reached once $\varphi^{(s)}$ has equilibrated; the early-time response, with $\varphi^{(s)}$ still unrelaxed, is carried by the larger unrelaxed modulus M^{-}. In the local limit $\Lambda\to 0$ ($l\ll h$), equation (65) gives $\varphi^{(s)}\approx[B^{-}/(3A^{-})]\,\partial_z\,u^{(s)}$, and substituting into (66) shows that the effective oedometric modulus is reduced to $M^{-}_{eff}:=M^{-}(1_\beta_B)$, yielding the closed-form consolidation coefficient

$$c_v^{\mathrm{eff}} = k\,\bar{M}(1-\beta_B) \qquad \beta_B := \frac{\bar{B}^2}{3\bar{M}\bar{A}}, \tag{68}$$

Using the definitions (59), the effective oedometric modulus admits the compact form

$$\bar{M}_{\mathrm{eff}} = \bar{M}(1-\beta_B) = \bar{M} - \frac{\bar{B}^2}{3\bar{A}} = \left(\lambda^{(s)}+2\mu^{(s)}\right) - \frac{\left(b^{(s)}\right)^2}{a^{(s)}} \tag{69}$$

since

$B^{-2}/(3A^{-})=(a^{(s)}+b^{(s)})2/a^{(s)})=a^{(s)}+2b^{(s)}+(b^{(s)})^2/a^{(s)}$ exactly cancels the microdilatation contribution $2b^{(s)}+a^{(s)}$ in M^{-}. Positive-definiteness of the free energy (90) requires $a^{(s)}>0$ and $(b^{(s)})^2< a^{(s)}(\lambda^{(s)}+2\mu^{(s)})$, so that $0<\bar{M}_{eff}\leq\lambda^{(s)}+2\mu^{(s)}$, with equality only when $b^{(s)}=0$. Consequently

$$c_v^{\mathrm{eff}}=k\bar{M}_{eff}\leq k(\lambda^{(s)}+2\mu^{(s)})=c_v^{\mathrm{cl}}, \tag{70}$$

i.e. in the local, fully relaxed limit the microdilatation coupling reduces the effective consolidation coefficient relative to the classical Terzaghi value. This is the relaxed-modulus behavior: once $\varphi^{(s)}$ has equilibrated (at late times $t\gg\tau_\varphi$, or in the elliptic limit $R\to 0$), the grain-level dilatation acts as an additional compliant mechanism that softens the equilibrium volumetric response of the skeleton to $\bar{M}_{eff}$. For $\Lambda>0$ or $R>0$ the system must be solved numerically as a coupled parabolic–parabolic problem.

Boundary and initial conditions

$(z=0: \&u^{(s)}=0, u^{(f)}=0, \partial_z\,\varphi^{(s)}=0$ (71)

(rigid impermeable base,no microdilatation flux)

$(z=h: T_{zz}^{(s)})+s^{(s)}=-q,\ p_{th}=0, m_z^{(s)}=0$ (72)
(applied load,drained surface,free microdilatation)

$$u^{(s)}(z,0)=u^{(f)}(z,0)=0,\ \varphi^{(s)}(z,0)=0. \quad (73)$$

At $t=0^+$, the undrained response of the incompressible constituents gives a uniform excess pore pressure equal to the applied load, p_th $(z,0^+)=q$, the classical Terzaghi initial condition. Because (65) is now a genuine evolution equation, $\varphi^{(s)}$ carries its own initial condition: the grain structure has not yet rearranged, so $\varphi^{(s)}(z,0)=0$ (unrelaxed). The skeleton therefore responds initially at the unrelaxed modulus M^-, softening to M^-_{eff} as $\varphi^{(s)}$ develops over τ_φ.

Characteristic scales and limiting cases
Equation (65) introduces one new characteristic length scale. Balancing the gradient term $c_1^{(s)}\partial_{zz}\varphi^{(s)}$ against the reaction term $3A^-\varphi^{(s)}$ defines the microdilatation length scale

$$\ell := \sqrt{c_1^{(s)}/(3\bar{A})} \quad (74)$$

and the dimensionless ratio

$$\Lambda := \ell/h = \sqrt{c_1^{(s)}/(3\bar{A})}/h, \quad (75)$$

The dissipative term in (65) introduces a second characteristic scale, absent from the elliptic theory: the microdilatation relaxation time

$$\tau_\varphi := \omega^{(s)}/(3\bar{A}) \quad (76)$$

the intrinsic time over which the grain-scale dilatation equilibrates, and the second dimensionless group

$$R := \tau_\varphi/t_c = \omega^{(s)}/(3\bar{A}\,t_c) \qquad t_c = h^2/c_v \quad c_v = k\bar{M}, \quad (77)$$

The response is governed by the two dimensionless numbers Λ and R; the elliptic theory is recovered as $R\to 0$, in which $\varphi^{(s)}$ relaxes instantaneously and M^-_{eff} governs from t=0+. When $\Lambda\ll 1$ the microdilatation is spatially quasi-uniform and $\varphi^{(s)}\approx[B^-/(3A^-)]\partial z u^{(s)}$ pointwise; when $\Lambda=O(1)$ a boundary layer of thickness l forms near the drained surface, where the sharp pore-pressure gradient makes $\varphi^{(s)}$ deviate from its local quasi-uniform value; at the impermeable base $\partial_z p_{th}=0$, so the local solution already satisfies the microdilatation flux condition there and no boundary layer forms.
In the doubly degenerate limit $a^{(s)}=b^{(s)}=0$ (hence $M^-\to\lambda^{(s)}+2\mu^{(s)}$, $B^-\to 0$, $A^-\to 0$), $\varphi^{(s)}$ vanishes identically and (67) reduces exactly to the classical Terzaghi equation

$$\partial_t p_{th} = c_v^{cl}\,\partial_{zz} p_{th} \qquad c_v^{cl} = k\left(\lambda^{(s)} + 2\mu^{(s)}\right) \quad (78)$$

confirming that microdilatational mixture theory contains classical poroelastic consolidation as a special case. When the microdilatation moduli vanish, $a^{(s)}=b^{(s)}=c_1^{(s)}=0$, the balance (65) degenerates to 0=0, $\varphi^{(s)}$ decouples and vanishes, and the length scale l is undefined. Equation (67) then reduces to (78), confirming that the coupling between pore-pressure diffusion and grain-level dilatation is a genuine microdilatation effect absent from classical poroelasticity.

Physical interpretation: two time scales and secondary compression
The response is set by two time scales, the drainage time $t_c=h^2/c_v$ and the microdilatation relaxation time $\tau_\varphi=\omega^{(s)}/(3A^-)$, together with the length scale l. The grain-scale dilatation now acts as a genuine internal relaxation mechanism. At early times ($t\ll\tau_\varphi$) the grains have not yet rearranged, $\varphi^{(s)}\approx 0$, and the skeleton carries the load at the unrelaxed modulus $\bar{M}=\lambda^{(s)}+2\mu^{(s)}+a^{(s)}+2b^{(s)}$; over τ_φ the dilatation develops and softens the skeleton to the relaxed modulus $\bar{M}_{eff}=(\lambda^{(s)}+2\mu^{(s)})-(b^{(s)})^2/a^{(s)}$ of (69), driving additional compaction. This stiff-to-soft transition, asserted but not realized by the elliptic theory, is an exact consequence of the

parabolic balance (65).

Two regimes follow from the ratio $R=\tau_\varphi/t_c$. When $R\lesssim 1$ the two scales overlap and the relaxation is absorbed into a single, drainage-controlled settlement at the reduced coefficient c_v^eff=k$\bar{M}_{eff}$. When $R\gg 1$ the scales separate: primary consolidation, controlled by drainage, completes over t_c at the stiff modulus $\bar{M}$; thereafter the microdilatation continues to relax over the much longer τ_φ, softening the skeleton to $\bar{M}_{eff}$ and producing continued settlement after the excess pore pressure has dissipated. This delayed, drainage-independent settlement is secondary compression, exactly the phenomenon that elastic Terzaghi–Biot theory, and the elliptic ($R\to 0$) limit of the present theory, cannot reproduce: in both, all compaction is slaved to pore-pressure dissipation and ceases with it. It is, on the other hand, the defining behavior of the classical rheological secondary-consolidation models (Gibson & Lo, 1961; Taylor & Merchant, 1940), to which the present local-limit response reduces (Section 6.6).

It is worth stating the motivating puzzle precisely. Classical consolidation does reproduce compaction continuing for years after the aquifer head stabilizes, provided the aquitard is thick and of low permeability, since the drainage time $t_c=h^2/c_v$ is then itself of order years to decades. What classical theory cannot reproduce is compaction that continues after the excess pore pressure has drained away, the residual, creep-like settlement documented in heavily pumped aquifer systems (Galloway & Burbey, 2011; Ojha et al., 2019) and conventionally described by empirical secondary-compression or elastic–viscoplastic rheology. The present theory supplies a thermodynamically consistent, grain-scale origin for that residual settlement: a single dissipative internal variable with a physical relaxation time τ_φ, calibratable against the same extensometer and head records. The spatial boundary-layer structure of $\varphi^{(s)}$, set by l through (65), further modifies the pore-pressure profile near the drained boundary, an effect absent from classical Terzaghi theory and from the local limit $a^{(s)}=b^{(s)}=0$.

Numerical results

The coupled parabolic–parabolic system (67), (65) is written in the dimensionless variables Z = z/h, T = t/tc, P = pth/q and F = Ƀφ$^{(s)}$/q, in which it depends only on βB, Λ and R. It is discretized by second-order central differences on a uniform grid of NZ = 161 nodes in Z ∈ [0, 1], with ghost-node (zero-flux) conditions at the impermeable base and for the microdilatation flux at the drained surface, and with the Dirichlet condition P = 0 at Z = 1. Time integration uses the fully implicit backward-Euler scheme, in which the microdilatation evolution equation and the consolidation equation are advanced simultaneously as one 2NZ × 2NZ sparse block linear system per step; the steps are distributed logarithmically (200 steps per decade of T), so that both the early drainage transient and the late secondary stage are resolved. The initial state is the undrained response pth(z,0$^+$) = q, $\varphi^{(s)}$(z,0) = 0 of (73). In the elliptic limit R = 0 the microdilatation equation is solved as a constraint at every step. The settlement is obtained by trapezoidal integration of the strain.

We consider a fine-grained interbed with dimensional parameters representative of the San Joaquin Valley, California, the best-documented aquifer system for pumping-induced land subsidence (Galloway & Burbey, 2011; Ojha et al., 2019; Poland, 1984): a singly-draining aquitard of thickness h=20 m, vertical hydraulic conductivity $K_v=1\times10^{(-9)}$ m s$^{(-1)}$, and a head decline Δh=30 m imposing a boundary pore-pressure step $\Delta p_0=\gamma_w\,\Delta h\approx 0.29$ MPa. The microdilatation moduli $a^{(s)}=0.5(\lambda^{(s)}+2\mu^{(s)})$, $b^{(s)}=0.3(\lambda^{(s)}+2\mu^{(s)})$ satisfy the positive-definiteness bound of (69) and give $\beta_B=0.61$; with $\lambda^{(s)}+2\mu^{(s)}=10$ MPa this yields an unrelaxed modulus $\bar{M}=\lambda^{(s)}+2\mu^{(s)}+a^{(s)}+2b^{(s)}=21$ MPa and a relaxed modulus $M^{-}_{eff}=8.2$ MPa. The drainage time at the unrelaxed stiffness is $t_c=h^2/(k\bar{M})\approx 6$ yr, so

the classical (relaxed-limit) response time is $t_c^{eff}=h^2/(k\bar{M}_{eff})\approx 15\,yr$; these are the observed decade-scale response times of San Joaquin Valley interbeds (Lees et al., 2022; Ojha et al., 2019; Poland, 1984). The relaxation time $\tau_\varphi=\omega^{(s)}/(3A^-)$ is the new material parameter; we report the dimensionless response versus $R=\tau_\varphi/t_c$, taking R=0,1,3,10,100 to span the regimes. The value $R\approx 3$ ($\tau_\varphi\approx 18\,yr$) is representative of the decadal residual compaction of San Joaquin interbeds, whereas R=100 is an idealized extreme that separates the two stages most cleanly. We use Λ=0.1 for the settlement, for which the internal length scale is negligible; it controls the boundary-layer structure, not the settlement magnitude. The complete parameter set and the derived quantities are listed in (Tab. 4).

Table 4: Parameters of the San Joaquin Valley-type example and derived quantities.

Quantity	Symbol	Value	Unit
Aquitard thickness (single drainage)	h	20	m
Vertical hydraulic conductivity	K_v	1×10^{-9}	m s^{-1}
Unit weight of water	γ_w	9.81	kN m^{-3}
Hydraulic mobility	$k=K_v/\gamma_w$	1.02×10^{-13}	m4 N^{-1} s^{-1}
Head decline; pressure step	Δh; $\Delta p_0=\gamma_w\Delta h$	30; 0.294	m; MPa
Drained oedometric modulus	$\lambda^{(s)}+2\mu^{(s)}$	10	MPa
Microdilatation moduli	$a^{(s)}$; $b^{(s)}$	5; 3	MPa
Unrelaxed modulus; relaxed modulus	$\bar{M}$; $\bar{M}_{eff}$	21; 8.2	MPa
Coupling and microdilatation moduli	$\bar{B}$; $\bar{A}$	24; 15	MPa
Coupling ratio	$\beta B=\bar{B}2/(3\bar{M}\bar{A})$	0.610	–
Drainage time (unrelaxed; relaxed)	t_c; t_c^{eff}	5.9; 15.2	yr
Primary and ultimate settlement	$\Delta p0h/\bar{M}$; $\Delta p0h/\bar{M}_{eff}$	28.0; 71.8	cm
Relaxation-time ratio (San Joaquin case)	$R=\tau_\varphi/t_c$	0, 1, 3 ($\tau\varphi\approx 18$ yr), 10, 100	–
Length ratio	$\Lambda=\ell/h$	0.1 ($\ell=2$ m); 0.25 in Section 6.7	–

The solver was verified in two ways. First, in the limit $R=0$, $\Lambda\to 0$ the system reduces exactly to Terzaghi consolidation with coefficient $(1-\beta_B)c_v$, whose settlement $S/(\Delta p0h/\bar{M}) = U[(1-\beta_B)T]/(1-\beta_B)$ follows from the classical series solution $U(T)=1-\Sigma\,2M^{-2}\exp(-M^2T)$, $M=\pi(2m+1)/2$. Table 5 compares the numerical and analytical settlements for the classical case ($\beta_B=0$) and for the present coupling ($\beta_B=0.61$); the relative error does not exceed 0.15% at any time and is dominated by the first-order time discretization. Second, Table 6 reports the settlement of the San Joaquin case (R = 3, Λ = 0.1) at t/tc = 1 and 10 for four grids and three time-step densities. The spatial discretization error is below 10^{-5}, and halving the time step changes the settlement by less than 0.2%, which confirms that the results reported below are converged to graphical accuracy.(Tab. 5 and 6)

Table 5: Verification against the analytical Terzaghi solution (R = 0, $\Lambda\to 0$; NZ = 161, 200 steps per decade).

βB	t/tc	Analytical $S/(\Delta p0h/\bar{M})$	Numerical $S/(\Delta p0h/\bar{M})$	Relative error (%)
0	0.05	0.2523	0.2521	0.07
0	0.2	0.5041	0.5037	0.08
0	0.5	0.7640	0.7629	0.14

0	1	0.9313	0.9301	0.13
0	2	0.9942	0.9938	0.04
0.61	0.05	0.4038	0.4035	0.06
0.61	0.2	0.8076	0.8070	0.07
0.61	0.5	1.2757	1.2747	0.08
0.61	1	1.7689	1.7667	0.12
0.61	2	2.2587	2.2555	0.14

Table 6: Mesh and time-step convergence of the settlement $S/(\Delta p0h/\bar{M})$ for the San Joaquin case ($R = 3$, $\Lambda = 0.1$, $\beta B = 0.61$).

Nodes N_z	Time steps per decade	$t/t_c = 1$	$t/t_c = 10$
41	50	1.0136	2.0508
41	100	1.0156	2.0550
41	200	1.0166	2.0571
81	50	1.0135	2.0508
81	100	1.0156	2.0550
81	200	1.0166	2.0571
161	50	1.0135	2.0508
161	100	1.0156	2.0550
161	200	1.0166	2.0571
321	50	1.0135	2.0508
321	100	1.0156	2.0550
321	200	1.0166	2.0571

(Fig. 3) shows the settlement, normalized by the primary (unrelaxed) compaction $\Delta p_0 h/\bar{M} \approx 28$ cm. Two features are central. First, the theory is a strict generalization: as $R \to 0$ (instantaneous relaxation) it reduces exactly to Terzaghi consolidation at the relaxed modulus $\bar{M}_{eff}$, reaching the ultimate settlement $S_\infty = \Delta p_0 h/\bar{M}_{eff} \approx 72$ cm (a factor $1/(1-\beta_B) = 2.6$ above the primary value) over t_c^eff. Second, and distinctively, when the relaxation is slow enough ($R \gtrsim 10$) the settlement is clearly two-stage (Fig. 3a): primary consolidation completes over t_c at the stiff modulus $\bar{M}$, giving a plateau near the primary compaction ≈28 cm, after which the microdilatation relaxes over τ_φ and secondary compression carries the settlement toward 72 cm. At smaller R the two scales overlap and no flat plateau forms: for the San Joaquin–representative case $R \approx 3$ ($\tau_\varphi \approx 18$ yr), secondary compression already begins before primary consolidation is complete (by $t \approx 2 t_c$ the settlement has reached only ≈1.2 times the primary compaction), and the residual, drainage-independent settlement then develops over the following few decades, in line with the observed decadal compaction. The idealized case R=100 (Fig. 3b) makes the mechanism explicit by separating the scales: the layer is essentially fully drained by $t \approx 2 t_c$ (mean excess pressure below 1% of Δp_0), yet the settlement continues to grow for a further two orders of magnitude in t/t_c. This continued, drainage-independent compaction is not reproduced by elastic Terzaghi–Biot consolidation at any single modulus; it is, however, precisely the behavior of the classical rheological secondary-consolidation models of Taylor and Merchant (1940) and Gibson and Lo (1961). In the spatially local limit $\Lambda \to 0$ used here, the coupled system (67), (65) is exactly Terzaghi drainage of a skeleton with a standard-linear-solid rheology unrelaxed modulus $\bar{M}$, relaxed modulus $\bar{M}_{eff}$, relaxation time τ_φ which is the Gibson–Lo model. The contribution here is

therefore not the two-stage settlement curve itself, but its derivation from a grain-scale degree of freedom within a thermodynamically consistent mixture theory, together with the internal length scale that a spatially local rheology does not possess, whose observable consequences the pore-pressure boundary layer and the seasonal phase lag are examined next.

We emphasize what is and is not a prediction here. The ultimate settlement, $\Delta p0\ h/\bar{M}_{eff}$, is fixed by the relaxed modulus alone, which an oedometer measures directly; a classical Terzaghi model calibrated to the same $\bar{M}_{eff}$ therefore gives the identical ultimate settlement, and the ultimate magnitude is not in itself a discriminating prediction. What elastic Terzaghi–Biot theory cannot reproduce, at any modulus, is the two-stage time course; but a classical rheological model reproduces it equally well, so the two-stage curve alone does not distinguish the present theory from that phenomenology. The distinguishing content lies instead in the internal length scale—the pore-pressure boundary layer and the seasonal phase lag of Section 6.7 which a spatially local rheological model does not contain. Note also that the microdilatation settlement is larger than the primary value at every instant, and slower only in the sense that a larger ultimate settlement takes longer to attain; the compaction rate itself is never below the classical primary rate. Finally, the coupling β_B=0.61 adopted here is a deliberately strong illustrative value, chosen so that the two stages are well separated in (Fig. 3); realistic aquitards have smaller β_B, hence a weaker relaxation and a smaller secondary-to-primary settlement ratio, for which the two-stage character persists but is less pronounced.

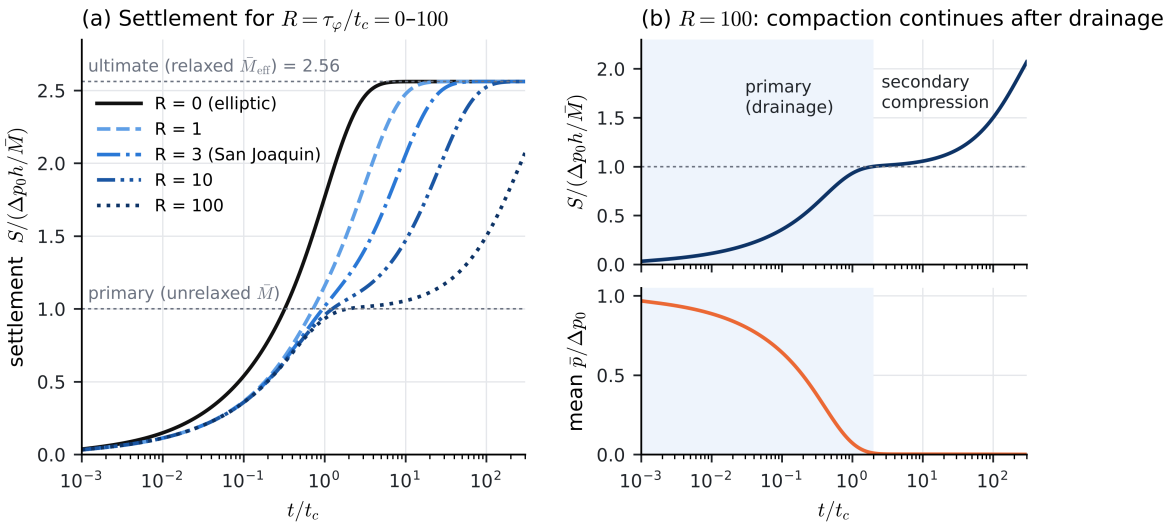


Figure 3: Two-stage consolidation of a microdilatational aquitard with a relaxing (dissipative) grain-scale dilatation, in dimensionless form (t/tc, tc = h2/(kM); settlement normalized by the primary compaction Δp0h/ M̄), for βB = 0.61 (M̄eff/M̄ = 0.39) and Λ = 0.1. (a) Settlement versus time for R = τφ/tc = 0, 1, 3, 10 and 100 (the case R = 3, τφ ≈ 18 yr, is representative of the decadal San Joaquin residual). The R = 0 curve is the elliptic limit, a single-stage consolidation to the relaxed ultimate 1/(1 − βB) = 2.56; a clear plateau near the primary (unrelaxed) value 1 appears only for R ≳ 10, followed by secondary compression to the same ultimate over τφ, whereas at smaller R (e.g. the San Joaquin case R = 3) the two stages overlap. (b) R = 100: settlement (upper panel) and mean excess pore pressure (lower panel) on a common time axis; the shaded band marks primary consolidation. The excess pore pressure drains to below 1% of Δp0 by t ≈ 2tc, yet the settlement keeps rising for a further two orders of magnitude in t/tc: the secondary-compression stage that elastic Terzaghi–Biot theory cannot produce (and that the local limit of the present theory shares with the classical Gibson–Lo rheological model).

Cyclic loading: seasonal pumping and the phase of the response

The analysis above concerns a monotonic head decline. In many exploited aquifer systems the dominant forcing is instead cyclic: seasonal pumping and recharge drive an annual oscillation of the aquifer head, and the aquitard compaction, and hence the land surface, oscillates in response. This seasonal deformation, now routinely resolved by InSAR and GPS, lags the head forcing by a measurable delay that has been used to infer aquifer properties (Chaussard et al., 2014; Smith & Vajedian, 2025). We ask whether the grain-scale dilatation, and in particular its relaxation time τ_φ, leaves a signature in the cyclic response distinct from classical consolidation.

We replace the step forcing by a harmonic boundary pore pressure $p_{th}(h,t)=\Delta p_0 \sin(\omega t)$ and solve the coupled system (65) and (67) to its periodic steady state, characterizing the response by the amplitude and phase lag of the depth-integrated compaction relative to the forcing, as functions of the dimensionless frequency ωt_c. Because the total overburden stress is held constant, the depth-integrated compaction is proportional to the depth-integrated pore-pressure response, so its phase is that of the land-surface response.

For the classical Terzaghi limit a semi-infinite diffusive layer under harmonic forcing has

$p_{th}(z,t)=\Delta p_0 e^{-\kappa z} \sin(\omega t-\kappa z)$ with $\kappa=\sqrt{(\omega/2c_v)}$, so that

$$\int_0^\infty e^{-\kappa z}\sin(\omega t-\kappa z)\,dz=\frac{1}{\kappa\sqrt{2}}\sin\left(\omega t-\frac{\pi}{4}\right) \qquad (79)$$

i.e. the phase lag is exactly $\pi/4=45^\circ$, at every frequency. This 45° figure is the semi-infinite limit; for a layer of finite thickness with an impermeable base the classical lag is not bounded by it, and overshoots slightly, peaking near $\approx 46.6^\circ$ at $\omega t_c \approx 8$ before settling back to 45° at high frequency (Fig. 4). The relevant classical reference for a single interbed is therefore $\approx 46.6^\circ$, not 45°.

Figure 4 shows the computed response. The microdilatation cases exceed the classical finite-layer bound through two mechanisms. The elliptic (R=0) limit already exceeds it by the non-local effect of the internal length scale, reaching ≈ 49–51° ($\Lambda=0.10$) and $\approx 54^\circ$ ($\Lambda=0.25$). The dissipative extension adds a second, temporal contribution: when the forcing period is comparable to the relaxation time, $\omega\tau_\varphi=O(1)$, the grain-scale dilatation lags the loading and further enhances the phase lag, to $\approx 54^\circ$ at $\Lambda=0.10$ and up to $\approx 57^\circ$ near $R\approx 0.1$–0.2 (Fig. 4b). The relaxation contribution is non-monotonic in R: it is maximal when τ_φ is a few tenths of t_c and vanishes both as $R\to 0$ (instantaneous relaxation) and as $R\to\infty$ (the dilatation frozen over a season), returning the lag to its finite-layer classical value.

This cyclic signature must be interpreted with care. In a real aquifer system the observed seasonal delay also reflects multi-layer structure and the coarse-grained fraction of the aquifer, and a purely elastic (classical) model can already push it to comparable values; Smith and Vajedian (2025), for instance, report elastic seasonal delays of up to ~60 days ($\approx 59^\circ$ on an annual cycle) from geometric effects alone. The microdilatation and geometric mechanisms both enhance the seasonal lag and are therefore confounded in field data: an observed lag exceeding 45° does not by itself establish microdilatation behavior. What the present analysis establishes is that grain-scale dilatation supplies a distinct, thermodynamically grounded mechanism, with both a length-scale and a relaxation-time signature, and that for a given, independently constrained aquitard geometry it predicts a larger phase lag than classical consolidation of the same layer. Discriminating the mechanisms would require independent constraints on the aquifer geometry, or multi-frequency deformation data able to separate their frequency signatures, a promising direction for combining the present theory with seasonal In-

SAR observations.

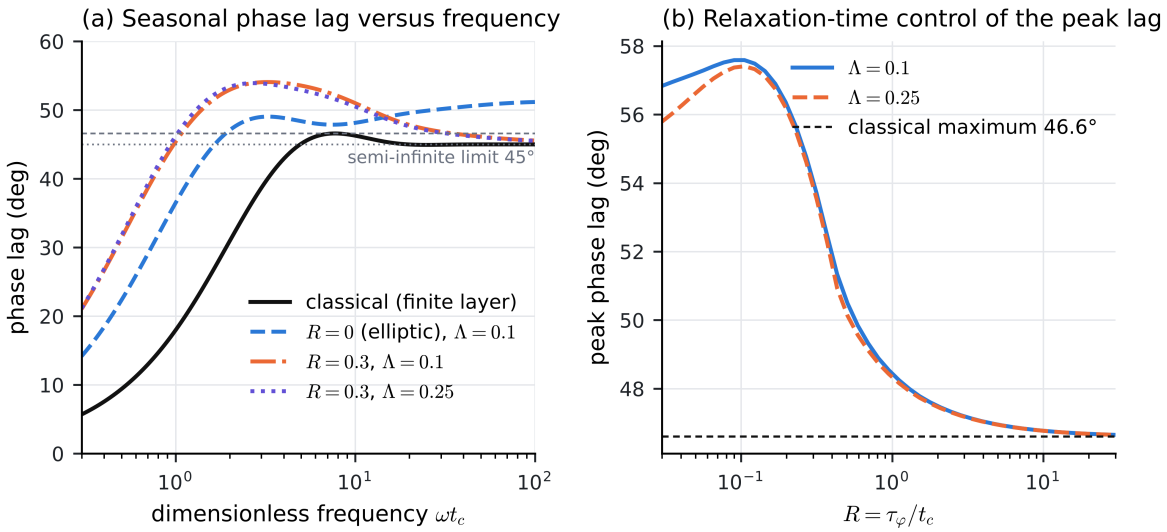


Figure 4: Seasonal phase lag of the depth-integrated compaction under harmonic boundary forcing, in the periodic steady state (βB = 0.61). (a) Phase lag versus dimensionless frequency ωtc: the classical finite-layer reference (solid) peaks at ≈ 46.6° near ωtc ≈ 8, not at the semi-infinite 45° limit (dotted); the elliptic microdilatation limit (R = 0, Λ = 0.1) reaches ≈ 49° near ωtc ≈ 3 and ≈ 51° at ωtc = 100, and the dissipative cases (R = 0.3) reach ≈ 54°. (b) Peak phase lag versus the relaxation-time ratio R = τφ/tc: the relaxation enhances the lag maximally near R ≈ 0.1–0.2 (up to ≈ 57.6°) and returns it to the classical 46.6° as R → ∞. As discussed in the text, geometric effects in a real multi-layer system can also raise the classical lag, so the mechanisms are confounded in field data.

Internal length scale and the pore-pressure boundary layer

The settlement curves of (Fig. 3) were computed for Λ = 0.1, for which the internal length has a negligible effect on the integrated compaction. Its effect on the pore-pressure field is shown in Fig. 5, which compares the isochrones of the local limit (Λ → 0) with those for Λ = 0.25. In the local elliptic limit (Fig. 5a) the microdilatation relaxes instantaneously and pointwise, and the isochrones are those of Terzaghi consolidation at the relaxed coefficient. A finite internal length (Fig. 5b) couples the grain-scale dilatation non-locally: the dilatation generated by drainage near the top boundary is transmitted over a distance of order l into the still-undrained interior, where it compresses the pore fluid before the fluid can escape. The excess pore pressure therefore rises transiently above its initial value Δp0 near the impermeable base, by up to 2.6% for Λ = 0.1 and 10.8% for Λ = 0.25 at t ≈ 0.12–0.14 tc. This non-monotonic response is analogous to the Mandel–Cryer effect of three-dimensional poroelasticity, but it is produced here in one dimension by the microstructure.

The dissipative relaxation suppresses the overshoot. For R ≥ 0.1 the grain structure cannot follow the drainage front quickly enough, the transient rise disappears (Fig. 5c), and the influence of Λ on the isochrones becomes markedly weaker. The pore-pressure signature of the internal length is therefore strongest when relaxation is fast compared with drainage (R ≪ 1), the same regime in which the seasonal phase lag of Section 6.7 is most enhanced. Piezometric profiles across thick interbeds, with closely spaced sensors near the impermeable boundary, would provide a direct test of this prediction. (Fig. 5)

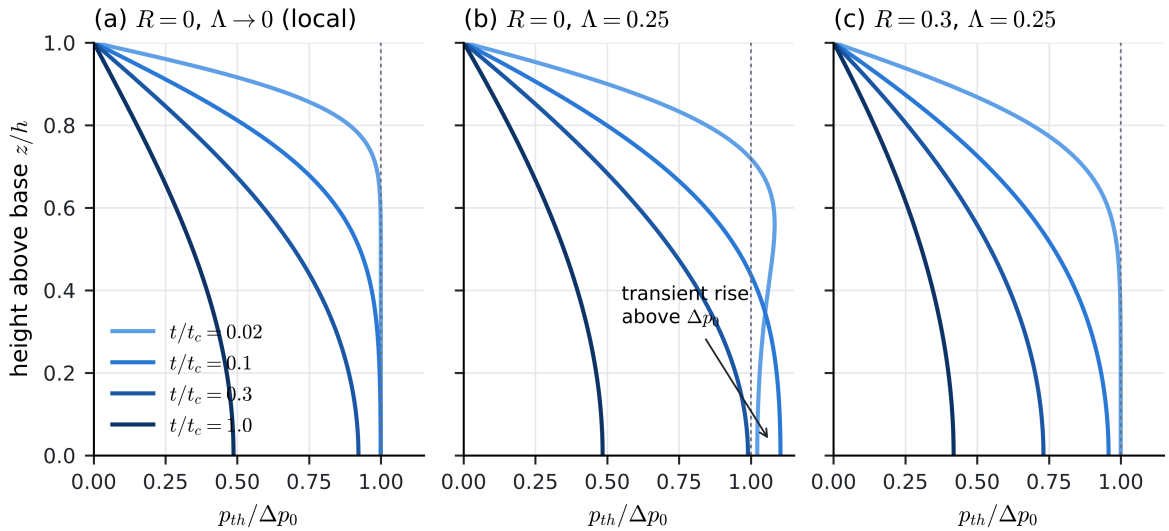


Figure 5: Excess pore-pressure isochrones pth (z, t)/Δp0 at t/tc = 0.02, 0.1, 0.3 and 1 (βB = 0.61). (a) Local elliptic limit (R = 0, Λ → 0), identical to Terzaghi consolidation at the relaxed coefficient. (b) Elliptic limit with internal length Λ = 0.25: the non-local dilatation produces a transient rise of the pore pressure above Δp0 near the impermeable base (maximum 1.108 at t ≈ 0.12tc). (c) Dissipative case R = 0.3, Λ = 0.25: the finite relaxation time suppresses the overshoot. The dotted line marks the initial undrained pressure.

Parametric sensitivity and practical implications

Table 7 quantifies how the coupling ratio β_B and the relaxation ratio R control the time course of compaction (Λ = 0.1). Three measures are reported: the times t50 and t90 at which 50% and 90% of the ultimate settlement are reached, and the residual fraction, defined as the fraction of the ultimate settlement that accrues after the mean excess pore pressure has fallen below 1% of Δp0, i.e. the drainage-independent settlement. Three conclusions follow. First, the ultimate settlement depends on β_B alone, $S_\infty/(\Delta p0 h/\bar{M}) = 1/(1 - \beta_B)$, and not on R, consistent with Section 6.6. Second, the residual fraction grows monotonically with R and tends to β_B as $R \to \infty$ (21%, 40% and 61% for β_B = 0.2, 0.4 and 0.61 at R = 100). In the scale-separated limit the secondary-to-ultimate settlement ratio is therefore the coupling ratio itself, which offers a direct route to identifying β_B from extensometer records that resolve the end of primary consolidation. Third, the delay of the 90% settlement is controlled jointly by β_B and R: for the San Joaquin case (β_B = 0.61, R = 3), $t_{90} \approx 15.7 t_c \approx 93$ yr, compared with $2.2 t_c \approx 13$ yr in the elliptic limit, whereas for the weak coupling β_B = 0.2 the corresponding increase is only from 1.1tc to 3.4tc. These results have a direct practical implication. A subsidence forecast that assumes compaction to cease once the measured heads, or the computed excess pore pressures, have stabilized will underestimate the long-term settlement by up to the residual fraction of Table 7. Conversely, the three parameters that control this residual can be constrained independently: β_B from the ratio of unrelaxed to relaxed oedometric stiffness, τ_φ from long-duration consolidation tests or from the post-drainage compaction rate observed by extensometers, and l from the seasonal phase lag observed by InSAR or GPS (Chaussard et al., 2014; Smith & Vajedian, 2025). (Tab.7).

RESULTS AND CONCLUSION

We have developed a microdilatational mixture theory for a saturated mixture of a microdilatation solid skeleton and a non-polar elastic fluid, derived throughout from the principle of virtual power and closed thermodynamically by the

Table 7: Sensitivity of the compaction history to the coupling ratio βB and the relaxation ratio R (Λ = 0.1). Times are normalized by tc = h2/(kM̄); dimensional values are given for the San Joaquin case (tc = 5.9 yr).

β_B	R	$S_\infty/(\Delta p_0 h/\bar{M})$	t_{50}/t_c	t_{90}/t_c	t_{90} (yr)	Residual fraction (%)
0.20	0	1.25	0.25	1.07	–	1
0.20	1	1.25	0.30	1.79	–	3
0.20	3	1.25	0.31	3.39	–	9
0.20	10	1.25	0.31	9.44	–	18
0.20	100	1.25	0.31	87.7	–	21
0.40	0	1.67	0.33	1.42	–	1
0.40	1	1.67	0.53	3.44	–	3
0.40	3	1.67	0.59	8.02	–	9
0.40	10	1.67	0.63	24.3	–	30
0.40	100	1.67	0.64	233.9	–	40
0.61	0	2.56	0.52	2.17	13	1
0.61	1	2.56	1.27	6.44	38	3
0.61	3	2.56	2.30	15.7	93	9
0.61	10	2.56	5.85	48.4	287	30
0.61	100	2.56	51.6	469.4	2,779	61

Coleman–Noll procedure within the Theory of Porous Media. The theory adds a single ingredient to classical poroelasticity, a grain-scale dilatational degree of freedom, coupled to the pore fluid, and reduces exactly to Biot–Terzaghi poroelasticity, and to the theory of elastic materials with voids, in the appropriate limits. Its contribution is to carry this one grain-scale mechanism, consistently, from a single variational statement through to a closed set of thermodynamically admissible field and constitutive equations.

Applied to one-dimensional consolidation, and thence to pumping-induced aquitard compaction and land subsidence, the theory yields an effect that classical poroelasticity cannot contain. Because the grain-scale dilatation is dissipative, with a relaxation time τ_φ distinct from the drainage time t_c, consolidation proceeds in two stages: primary consolidation controlled by drainage, at the unrelaxed modulus M̄, followed by secondary compression as the grain structure relaxes to the softer modulus $\bar{M}_{eff}$. When $\tau_\varphi \gg t_c$ this secondary stage continues after the excess pore pressure has fully dissipated, reproducing the residual, creep-like compaction documented in heavily pumped aquifer systems. In its spatially local limit this two-stage response coincides with the classical rheological secondary-consolidation model of Taylor–Merchant and Gibson–Lo (Gibson & Lo, 1961; Taylor & Merchant, 1940); the present theory supplies that model's missing grain-scale, thermodynamically consistent origin, and adds an internal length scale that a spatially local rheology cannot contain. Under seasonal pumping this length scale, together with the relaxation, produces a phase lag that exceeds the classical finite-layer diffusion bound. In the appropriate limits the theory reduces exactly to the elliptic (instantaneous) microdilatation theory and to Biot–Terzaghi poroelasticity. It is these length-scale effects the pore-pressure boundary layer and the seasonal phase lag rather than the two-stage settlement it shares with rheological consolidation models, that distinguish the theory observationally.

The principal findings are as follows. (1) The theory reduces exactly to Biot–Terzaghi poroelasticity when the microdilatation moduli vanish, to the theory of elastic materials with voids when the fluid is removed, and to the elliptic microdi-

latation theory as $\omega^{(s)} \to 0$; the numerical solution reproduces the analytical Terzaghi solution to within 0.15%. (2) For a San Joaquin Valley-type aquitard (h = 20 m, Δh = 30 m, β_B = 0.61), the primary and ultimate settlements are 28 and 72 cm, and for R = 3 the 90% settlement is reached after approximately 93 yr, compared with 13 yr when the grain structure relaxes instantaneously. (3) The fraction of the ultimate settlement that develops after the excess pore pressure has dissipated increases with R and tends to β_B in the scale-separated limit. (4) The internal length scale produces a transient, Mandel–Cryer-type rise of the pore pressure at the impermeable base of up to 11% (Λ = 0.25) when relaxation is fast, and the combined length-scale and relaxation effects raise the peak seasonal phase lag from the classical finite-layer value of 46.6° to approximately 57.6° near R ≈ 0.1.

For practice, the results indicate that forecasts which assume compaction to stop once the excess pore pressure has dissipated may underestimate long-term subsidence in strongly coupled aquitards, and that the three additional constants of the theory can be constrained by standard measurements: oedometer tests (unrelaxed and relaxed moduli), long-duration consolidation or extensometer records (relaxation time) and seasonal InSAR deformation (internal length).

Several extensions are natural. The theory excludes mass exchange between constituents; admitting a mass-supply term in (5) would extend it to reactive or phase-changing microdilatation mixtures. The constitutive development is isotropic and hyper-elastic; anisotropic microdilatation response, or a fluid that itself carries microstructure, would broaden the range of applicable materials. The one-dimensional analysis of Section 6 rests on quasi-static loading, an incompressible fluid, and the Λ→0 local limit for the closed-form result; relaxing these is the natural next step. A fully dynamic treatment, in particular, would reveal the dispersive wave structure of the microdilatation mixture and allow the predicted wave speeds to be compared against ultrasonic measurements on saturated granular media. Finally, identifying the microdilatation constants, the moduli $a^{(s)}$, $b^{(s)}$,$c_1^{(s)}$ and the relaxation coefficient $\omega^{(s)}$ (equivalently $\bar{M}_{eff}$, the length $l=\sqrt{(c_1^{(s)})/(3A^-)}$, and the relaxation time $\tau_\varphi=\omega^{(s)}/(3A^-)$, by fitting the ultimate compaction, the boundary-layer structure, and above all the secondary-compression stage to oedometer, extensometer, and InSAR records, is the key step toward practical application.

REFERENCES

Atkin, R. J., & Craine, R. E. (1976). Continuum theories of mixtures: Basic theory and historical development. The Quarterly Journal of Mechanics and Applied Mathematics, 29(2), 209–244. https://doi.org/10.1093/qjmam/29.2.209

Bedford, A., & Drumheller, D. S. (1983). Theories of immiscible and structured mixtures. International Journal of Engineering Science, 21(8), 863–960. https://doi.org/10.1016/0020-7225(83)90071-X

Biot, M. A. (1941). General theory of three-dimensional consolidation. Journal of Applied Physics, 12(2), 155–164. https://doi.org/10.1063/1.1712886

Bowen, R. M. (1976). Theory of mixtures. In A. C. Eringen (Ed.), Continuum physics (Vol. 3, pp. 1–127). Academic Press. https://doi.org/10.1016/B978-0-12-240803-8.50017-7

Bowen, R. M. (1980). Incompressible porous media models by use of the theory of mixtures. International Journal of Engineering Science, 18(9), 1129–1148. https://doi.org/10.1016/0020-7225(80)90114-7

Chaussard, E., Bürgmann, R., Shirzaei, M., Fielding, E. J., & Baker, B. (2014). Predictability of hydraulic head changes and characterization of aquifer-system and fault properties from InSAR-derived ground deformation. Journal of Geophysical Research: Solid Earth, 119(8), 6572–6590. https://doi.org/10.1002/2014JB011266

Chiriţă, S., & Galeş, C. (2008). A mixture theory for microstretch thermoviscoelastic solids. Journal of Thermal Stresses, 31(11), 1099–1124. https://doi.org/10.1080/01495730802250847

Coleman, B. D., & Noll, W. (1963). The thermodynamics of elastic materials with heat conduc-

tion and viscosity. Archive for Rational Mechanics and Analysis, 13(1), 167–178. https://doi.org/10.1007/BF01262690

Cowin, S. C., & Nunziato, J. W. (1983). Linear elastic materials with voids. Journal of Elasticity, 13(2), 125–147. https://doi.org/10.1007/BF00041230

Del Piero, G. (2009). On the method of virtual power in continuum mechanics. Journal of Mechanics of Materials and Structures, 4(2), 281–292. https://doi.org/10.2140/jomms.2009.4.281

dell'Isola, F., & Placidi, L. (2011). Variational principles are a powerful tool also for formulating field theories. In F. dell'Isola & S. Gavrilyuk (Eds.), Variational models and methods in solid and fluid mechanics (CISM International Centre for Mechanical Sciences, Vol. 535, pp. 1–15). Springer. https://doi.org/10.1007/978-3-7091-0983-0_1

dell'Isola, F., Rosa, L., & Woźniak, C. (1998). A micro-structured continuum modelling compacting fluid-saturated grounds: The effects of pore-size scale parameter. Acta Mechanica, 127(1–4), 165–182. https://doi.org/10.1007/BF01170371

Diebels, S. (2002). Micropolar mixture models on the basis of the Theory of Porous Media. In W. Ehlers & J. Bluhm (Eds.), Porous media: Theory, experiments and numerical applications (pp. 121–145). Springer. https://doi.org/10.1007/978-3-662-04999-0_3

Diebels, S., & Ehlers, W. (1996). On fundamental concepts of multiphase micropolar materials. Technische Mechanik, 16(1), 77–88. https://journals.ub.ovgu.de/index.php/techmech/article/download/1218/1192/3715

Ehlers, W. (2002). Foundations of multiphasic and porous materials. In W. Ehlers & J. Bluhm (Eds.), Porous media: Theory, experiments and numerical applications (pp. 3–86). Springer. https://doi.org/10.1007/978-3-662-04999-0_1

Eringen, A. C. (1999). Microcontinuum field theories: I. Foundations and solids. Springer. https://doi.org/10.1007/978-1-4612-0555-5

Forest, S., & Sievert, R. (2006). Nonlinear microstrain theories. International Journal of Solids and Structures, 43(24), 7224–7245. https://doi.org/10.1016/j.ijsolstr.2006.05.012

Galloway, D. L., & Burbey, T. J. (2011). Review: Regional land subsidence accompanying groundwater extraction. Hydrogeology Journal, 19(8), 1459–1486. https://doi.org/10.1007/s10040-011-0775-5

Germain, P. (1973). The method of virtual power in continuum mechanics. Part 2: Microstructure. SIAM Journal on Applied Mathematics, 25(3), 556–575. https://doi.org/10.1137/0125053

Germain, P. (2020). The method of virtual power in the mechanics of continuous media, I: Second-gradient theory (M. Epstein & R. E. Smelser, Trans.). Mathematics and Mechanics of Complex Systems, 8(2), 153–190. https://doi.org/10.2140/memocs.2020.8.153 (Original work published 1973)

Gibson, R. E., & Lo, K. Y. (1961). A theory of consolidation for soils exhibiting secondary compression (Publication No. 41). Norwegian Geotechnical Institute.

Haghshenas Haghighi, M., & Motagh, M. (2024). Uncovering the impacts of depleting aquifers: A remote sensing analysis of land subsidence in Iran. Science Advances, 10(19), Article eadk3039. https://doi.org/10.1126/sciadv.adk3039

Herrera-García, G., Ezquerro, P., Tomás, R., Béjar-Pizarro, M., López-Vinielles, J., Rossi, M., Mateos, R. M., Carreón-Freyre, D., Lambert, J., Teatini, P., Cabral-Cano, E., Erkens, G., Galloway, D., Hung, W.-C., Kakar, N., Sneed, M., Tosi, L., Wang, H., & Ye, S. (2021). Mapping the global threat of land subsidence. Science, 371(6524), 34–36. https://doi.org/10.1126/science.abb8549

Hütter, G. (2020). Coleman–Noll procedure for classical and generalized continuum theories. In H. Altenbach & A. Öchsner (Eds.), Encyclopedia of continuum mechanics (pp. 316–323). Springer. https://doi.org/10.1007/978-3-662-55771-6_57

Ieşan, D., & Quintanilla, R. (2014). On a theory of thermoelastic materials with a double porosity structure. Journal of Thermal Stresses, 37(9), 1017–1036. https://doi.org/10.1080/01495739.2014.914776

Lees, M., Knight, R., & Smith, R. G. (2022). Development and application of a 1D compaction model to understand 65 years of subsidence in the San Joaquin Valley. Water Resources Research, 58(6), Article e2021WR031390. https://

doi.org/10.1029/2021WR031390
Maugin, G. A. (2017). Non-classical continuum mechanics: A dictionary (Advanced Structured Materials, Vol. 51). Springer. https://doi.org/10.1007/978-981-10-2434-4
Mindlin, R. D. (1964). Micro-structure in linear elasticity. Archive for Rational Mechanics and Analysis, 16(1), 51–78. https://doi.org/10.1007/BF00248490
Murad, M. A., Guerreiro, J. N., & Loula, A. F. D. (2001). Micromechanical computational modeling of secondary consolidation and hereditary creep in soils. Computer Methods in Applied Mechanics and Engineering, 190(15–17), 1985–2016. https://doi.org/10.1016/S0045-7825(00)00218-8
Nunziato, J. W., & Cowin, S. C. (1979). A nonlinear theory of elastic materials with voids. Archive for Rational Mechanics and Analysis, 72(2), 175–201. https://doi.org/10.1007/BF00249363
Ojha, C., Werth, S., & Shirzaei, M. (2019). Groundwater loss and aquifer system compaction in San Joaquin Valley during 2012–2015 drought. Journal of Geophysical Research: Solid Earth, 124(3), 3127–3143. https://doi.org/10.1029/2018JB016083
Poland, J. F. (Ed.). (1984). Guidebook to studies of land subsidence due to ground-water withdrawal (Studies and Reports in Hydrology No. 40). UNESCO. https://unesdoc.unesco.org/ark:/48223/pf0000065167
Qi, J., Xie, Y., Li, C., Guo, H., & Wang, Y. (2025). Creep behavior of clayey soil and its model prediction in the Cangzhou land subsidence area. Scientific Reports, 15, Article 9130. https://doi.org/10.1038/s41598-025-93928-z
Quiligotti, S., Maugin, G. A., & dell'Isola, F. (2003). An Eshelbian approach to the nonlinear mechanics of constrained solid–fluid mixtures. Acta Mechanica, 160(1–2), 45–60. https://doi.org/10.1007/s00707-002-0968-z
Smith, R. G., & Vajedian, S. (2025). How quickly does elastic deformation respond to seasonal changes in hydraulic head? Insights from modeling and field data in the western USA. Hydrogeology Journal, 33(2), 611–625. https://doi.org/10.1007/s10040-025-02891-6
Taylor, D. W., & Merchant, W. (1940). A theory of clay consolidation accounting for secondary compression. Journal of Mathematics and Physics, 19(1–4), 167–185. https://doi.org/10.1002/sapm1940191167
Terzaghi, K. (1943). Theoretical soil mechanics. Wiley. https://doi.org/10.1002/9780470172766
Truesdell, C. (1984). Rational thermodynamics (2nd ed.). Springer. https://doi.org/10.1007/978-1-4612-5206-1
Twiss, R. J., & Eringen, A. C. (1971). Theory of mixtures for micromorphic materials—I: Balance laws. International Journal of Engineering Science, 9(10), 1019–1044.
Wilson, R. K., & Aifantis, E. C. (1982). On the theory of consolidation with double porosity. International Journal of Engineering Science, 20(9), 1009–1035. https://doi.org/10.1016/0020-7225(82)90036-2

COPYRIGHTS
©2023 The author(s). This is an open access article distributed under the terms of the Creative Commons Attribution (CC BY 4.0), which permits unrestricted use, distribution, and reproduction in any medium, as long as the original authors and source are cited. No permission is required from the authors or the publishers.

HOW TO CITE THIS ARTICLE
Ghiasi Tarzi, A., Robati, A. & Kazerooni Sadi, M. A. (2026). A Micro-Dilatational Mixture Theory for Saturated Porous Media: From Virtual Power to Aquitard Compaction and Land Subsidence. (e743002). International Journal of Urban Management and Energy Sustainability, (), e743002

DOI: 10.22034/ijumes.2026.2109321.1427